ISSN 0027-1349, Moscow University Physics Bulletin, 2024, Vol. 79, Suppl. 2, pp. S935–S943. © Allerton Press, Inc., 2024.

Gaussian Process Based Prediction of Density Distribution in Core of Research Nuclear Reactor

N. V. Smolnikov[1]*, M. N. Anikin[1], A. G. Naimushin[1], and I. I. Lebedev[1]

[1] *National Research Tomsk Polytechnic University, Tomsk, Russia*

Received October 1, 2024; revised October 10, 2024; accepted October 20, 2024

Abstract—Research nuclear reactors operate in a partial refueling mode, which leads to the formation of local areas with high nonuniformity of power density distribution. Such areas impact the economic efficiency of fuel consumption and the reactor core reliability. This necessitates the power density distribution profiling and underscores the importance of identifying the patterns of power distribution formation within the heterogeneous structure of the reactor core. In this study, an analysis of the reactor's operational experience under various fuel loadings was conducted, and the characteristics of power density distribution in each cell were determined. An approach to applying a machine learning model for predicting power density distribution nonuniformity across the fuel cells of the IRT-T reactor core is presented. It is shown that the application of the supervised learning concept and Gaussian process regression with combined covariance (kernel) function enables the prediction of power distribution parameters in each reactor cell, regardless of the specific loading pattern and fuel burnup depth. The model achieved an overall accuracy of over 99%, with a mean absolute error not exceeding 0.5%.

Keywords: power density distribution, nuclear research reactor, IRT-T reactor, MCU-PTR, machine learning, supervised learning, gaussian process

DOI: 10.3103/S0027134924702394

INTRODUCTION

Large number of experimental facilities and the compact size of the reactor core make research nuclear reactors (RNRs) are essential tools for conducting fundamental and applied research in solid-state physics, neutron scattering, isotope production, materials science, and medicine. The compact size of the reactor core is achieved by using a small number of highly enriched fuel assemblies (FAs) and the placement of a neutron reflector. However, research nuclear reactors exhibit a high degree of heterogeneity of neutronic characteristics within the reactor core and the reflector, which is due to the following factors [1].

- The use of partial refueling mode, where only high discharge burnup FAs are refueled, leading to a local increase of power density in the cell with fresh fuel and a redistribution of power density across the core.

- The effect of a neutron reflector with a low neutron absorption cross-section, which increases the power density in the FAs located at the 'core-reflector' boundary, thereby enhancing the nonuniformity of power density distribution (PDD) across the fuel cells.

The neutron flux density distribution within the reactor core significantly impacts the reactor's multiplication properties and the temperature distribution across the fuel elements (fuel rods). In exceptional cases, significant flux heterogeneity can become a limiting factor for their operation due to the critical heat flux [2]. When partial refueling of the core lead to regions of high flux distribution heterogeneity, power distribution profiling is required, which is typically achieved by "fresh" FAs permutation from the core center to the periphery. The wide variety of combinations of FAs with different discharge burnup in the core of a reactor precludes the use of a standard power distribution profiling scheme due to the inherently unknown number of permutations. This necessitates a series of calculations and the development of a customized profiling scheme for each specific case. The present work is focused on determining the patterns of PDD in the reactor core and developing a machine learning model to predict PDD across fuel cells [3].

*E-mail: nvs38@tpu.ru

1. NUCLEAR RESEARCH REACTOR IRT-T

The IRT-T reactor is an intermediate-flux pool type RNR of thermal power of 6 MW, which was commissioned after a major upgrade in 1984 [4]. The reactor core consists of IRT-3M type FAs enriched up to 90%. The default core loading pattern consists of 11 eight-tube (8 fuel elements) and 9 six-tube (6 fuel elements) FAs. Beryllium metal, placed around the perimeter of the reactor core, is used as the neutron reflector. The reactor control and protection system consists of 9 control elements: three groups of compensating rods (CR-1, CR-2, CR-3), two safety rods (SR-1, SR-2), and an automatic regulating rod (AR). The reactor has 10 horizontal and 15 vertical experimental channels with diameters ranging from 42 to 180 mm (Fig. 1). The most intense experimental channels are located in the central neutron trap of the core and have a maximum thermal neutron flux density of 2×10^{14}n cm^{-2} s^{-1}. The average annual time on power is 3600 h. The length of the fuel cycle ranges from 25 to 35 effective full-power days.

For the IRT-T reactor, which operates in a partial refueling mode, the asymmetrical shape of the beryllium reflector (Fig. 1) also influences the power distribution across the fuel cells, leading to an increase in the power density of the fuel assemblies (FAs) located in the right part of the core. In general, the PDD, which characterizes the nonuniformity degree of power distribution nonuniformity, can be represented as Eq. (1):

$$K_v = K_Z K_{\text{cell}} K_{\text{fe}} = \frac{\Phi_Z^{\max}\Phi_{\text{cell}}^{\max}\Phi_{\text{fe}}^{\max}}{\Phi_Z^{\text{aver}}\Phi_{\text{cell}}^{\text{aver}}\Phi_{\text{fe}}^{\text{aver}}}, \qquad (1)$$

where $K_Z, K_{\text{cell}}, K_{\text{fe}}$—PDDs along height, cross-section and fuel elements of the reactor core, respectively; $\Phi_Z^{\max}\Phi_{\text{cell}}^{\max}\Phi_{\text{fe}}^{\max}$—maximum neutron flux density along height, cross-section and fuel elements of the reactor core, respectively; $\Phi_Z^{\text{aver}}\Phi_{\text{cell}}^{\text{aver}}\Phi_{\text{fe}}^{\text{aver}}$—average neutron flux density along height, cross-section and fuel elements of the reactor core, respectively.

Depending on the fuel loading pattern, the cells with "fresh" FAs and the average burnup, the PDD in the reactor core can exceed $K_v > 3.0$. The determination of the neutron flux density distribution, considering the heterogeneous structure, is based on Eq. (2), which is a function of four variables:

$$\Phi = \frac{1}{V}\int dE \int dt \int dV \int \Omega\nu n(\vec{r}, \Omega E, t), \quad (2)$$

where ν is the velocity cm/sh (1 sh = 10^{-8} s); $\vec{r}$ is the particle position vector, cm; Ω is the direction vector; E is the energy, MeV; t is the time, sh; V is the volume of the cell, cm^3.

From Eqs. (1) and (2), it follows that changes in the fuel loading due to the FAs permutations or core refueling lead to variations in neutron flux density and PDD throughout the reactor core.

To perform computational determination of neutronic parameters in the heterogeneous structure of the core elements, experimental devices, as well as to assess changes in the nuclide composition of the fuel, we do utilize the Monte Carlo particle transport code, MCU-PTR with the MDBPT50 constant library [5]. The full-scale reactor core model (Fig. 2) includes fuel elements, control and protection system components, vertical and horizontal experimental channels with more than 1500 total number of individual materials, which allows for pin-by-pin calculations of neutron fluxes, power distribution, and determination of radiation parameters in experimental facilities with high precision [6–8].

MCU-PTR code allows to compute Eq. (2) at any point within the reactor core and get Eq. (1) for the entire reactor core based on the current fuel loading pattern. However, to address the existing issue of power distribution nonuniformity, a series of independent calculations is required, where the cells for FA permutations select based on assumptions, since it is not initially known how the power distribution will be redistributed or how the power formation occurs in the core cells at different fuel burnup. As a result, the "permutation–simulation–analysis" cycle is considered, which represents a process that demands significant computational resources.

Similar problems have been addressed by research teams [9–14], focusing on optimizing the operation of reactor facility to enhance their efficiency and safety. However, the tasks in these studies were related to the core of a power reactor, which is part of a nuclear power plant and has significant design and operational differences from research reactors.

Thereby, an urgent task is to establish the characteristics of PDD formation across fuel cells of research reactor and to develop a predictive model for forecasting power distribution nonuniformity based on any core fueling pattern. This would simplify the process of selecting cells for FA permutations, aiming to reduce power peaking factor and achieve a more uniform power distribution.

2. POWER DENSITY DISTRIBUTION IN THE REACTOR CORE

Components of Eq. (1) take into account distribution of neutron flux along the height of the core, fuel elements and fuel cells. Considering Eq. (1) with each component varying independently significantly complicates determining the contribution attributed solely to the K_{cell} component. Therefore, for the

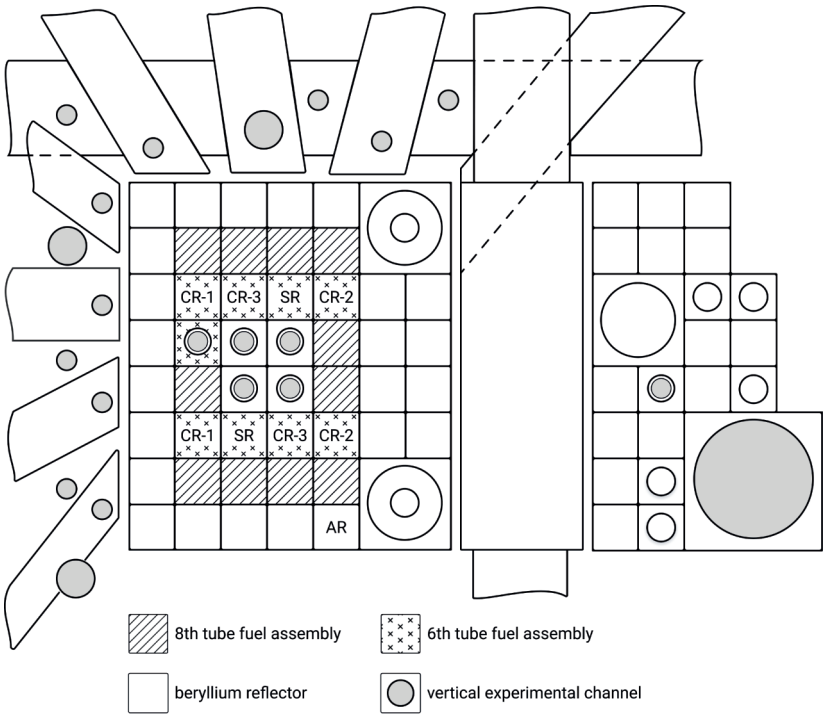

Fig. 1. IRT-T reactor core diagram.

purposes of analyzing the patterns of PDD formation, the coefficients of K_Z and K_{fe} are treated as constants for the entire reactor core. An example of the redistribution of power density across cells as a result of core refueling is presented in Fig. 3.

In case of uniform PDD ($K_{\text{cell}} = 1$), a thermal power of 6 MW would be achieved with each cell generating 300 kW. However, under actual operating conditions, involving partial core refueling and the use of an asymmetrical beryllium reflector, achieving absolute uniform conditions is not feasible. As shown in Fig. 3, the core refueling resulted in an average power density redistribution across all cells exceeding 15%, with the relative difference between the left and right sides of the core exceeding 16%. The PDD changed significantly, so additional permutations are required, which can only be achieved through the previously mentioned "permutation–simulation–analysis" cycle.

To establish the dependency of PDD formation in fuel cells, a dataset of core loading patterns containing over 500 unique fuel patterns were developed. Dataset includes more than 10 000 unique "burnup–PDD" pairs. The exploratory data analysis of some fuel cells is presented in Fig. 4.

As can be seen in Fig. 4, the proximity of a cell to the right side of the core results in higher power density in the FAs (cell 5-3). Although the burnup and PDD values exhibit a linear relationship, all fuel cells demonstrate variability, reflecting the influence of neighboring FAs (cells) on the PDD values.

For some fuel loading pattern the maximum difference in power density between cells 7-6 (peripheral) and 5-3 (most stressed) can reach factor of 3.4, which has a significant impact on the process of power distribution leveling within the reactor core. The average difference of PDD values for cells 7-6 and 5-3 exceeds a factor of 1.6.

The statistical relationship between the variables (fuel cells) was determined using Kendall's rank correlation coefficients and p-values of the null hypothesis H_0, which assumes no correlation [15, 16]. Both burnup and PDD values were considered as variables, forming a 40×40 square matrix. A part of the square matrix, containing the Kendall correlation coefficients and p-values is shown in Fig. 5.

The entire 40×40 matrix cannot be displayed, so the only some of them to show the relationships between FAs located in different parts of the core were selected. The results from the matrix in Fig. 4 indicate the following:

- There is a moderate correlation between adjacent cells with respect to the PDD parameter.
- Correlation between burnup and PDD shows that multiple cells simultaneously influence the power density values (for example, the PDD in cell 7-6_e is affected by distant cells 2-3_b,

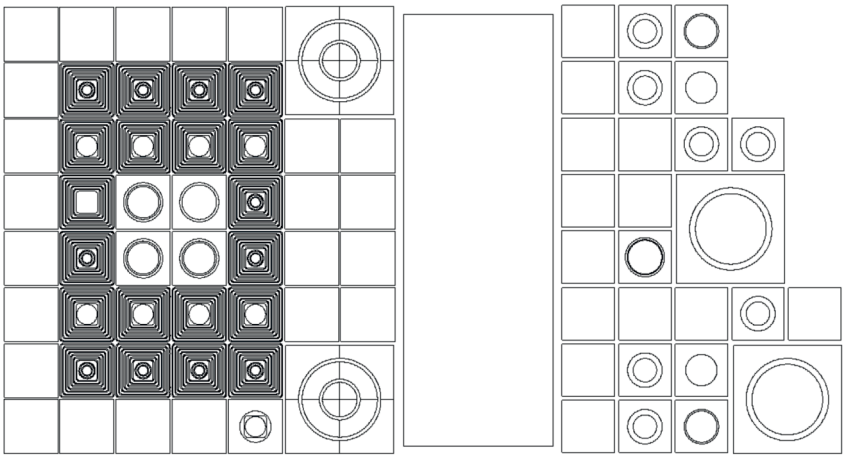

Fig. 2. Full-scale model of IRT-T reactor core.

Before refueling

Burnup, %

Cell*	6	5	4	3
7	13.23	9.58	41.41	49.68
6	33.20	58.42	26.37	32.60
5	59.14	Be	Be	41.00
4	67.02	Be	Be	40.28
3	32.47	23.94	57.97	31.17
2	13.07	41.01	9.54	47.55
	Burnup by sides, %			
	35.11		37.76	

PDD, rel.units

6	5	4	3	Cell
1.01	1.16	0.94	0.88	**7**
0.95	0.80	1.26	1.16	**6**
0.76	Be	Be	1.23	**5**
0.65	Be	Be	1.20	**4**
0.93	1.16	0.82	1.15	**3**
1.02	0.87	1.17	0.86	**2**
PDD by sides, rel.units				
0.93		1.07		

After refueling

Burnup, %

Cell*	6	5	4	3
7	13.23	9.58	41.41	49.68
6	33.20	58.42	26.37	32.60
5	0.00	Be	Be	41.00
4	0.00	Be	Be	40.28
3	32.47	23.94	57.97	31.17
2	13.07	41.01	9.54	47.55
	Burnup by sides, %			
	22.49		37.76	

PDD, rel.units

6	5	4	3	Cell
1.02	1.09	0.84	0.76	**7**
0.97	0.79	1.16	1.01	**6**
1.36	Be	Be	1.07	**5**
1.36	Be	Be	1.05	**4**
0.96	1.17	0.76	1.00	**3**
1.04	0.83	1.06	0.74	**2**
PDD by sides, rel.units				
1.08		0.92		

* Note to read 7-6 cell, where 7 and 6 are row and column, respectively

– spent / fresh FA

Fig. 3. PDD changes caused by refueling of spent fuel in cells 4–6 and 5–6.

2-4_b, 2-5_b), which is also confirmed by the presence of variability in Fig. 4.

- The pairs of "burnup–PDD" have strong negative correlation.
- When the correlation coefficient $|r| \geq 0.12$, the null hypothesis is rejected, which can be considered as a threshold value where the influence of one variable on another is significant.
- The evaluation of the dataset values showed that the PDD formation in each cell is unique, and even slight permutations lead to a redistribution of power density in the entire core.

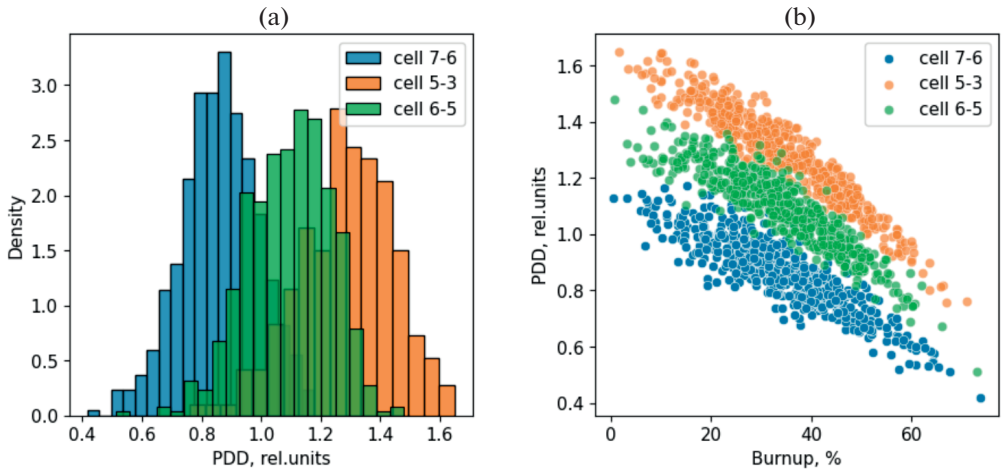

Fig. 4. Analysis of PDD and burnup features for some of reactor core cells: (a) histogram; (b) PDD vs burnup depth.

p-value

Kendall correlation coefficient (r)

Cell*	7-6_e	7-5_e	7-4_e	2-3_e	2-4_e	2-5_e	7-6_b	7-5_b	7-4_b	2-3_b	2-4_b	2-5_b
7-6_e		0.00	0.00	0.00	0.00	0.00	0.00	0.05	0.15	0.03	0.01	0.01
7-5_e	0.35		0.00	0.00	0.00	0.00	0.12	0.00	0.96	0.00	0.01	0.01
7-4_e	0.32	0.25		0.00	0.00	0.00	0.16	0.71	0.00	0.01	0.02	0.01
2-3_e	-0.38	-0.40	-0.34		0.00	0.00	0.02	0.00	0.02	0.00	0.08	0.36
2-4_e	-0.35	-0.42	-0.37	0.34		0.00	0.01	0.00	0.02	0.49	0.00	0.05
2-5_e	-0.34	-0.44	-0.37	0.25	0.40		0.02	0.00	0.02	0.94	0.06	0.00
7-6_b	-0.88	-0.08	-0.08	0.13	0.14	0.13		0.81	0.35	0.63	0.95	0.70
7-5_b	-0.09	-0.89	-0.03	0.15	0.21	0.17	0.01		0.25	0.27	0.47	0.17
7-4_b	-0.09	0.01	-0.88	0.12	0.15	0.16	0.04	-0.05		0.36	0.75	0.86
2-3_b	0.12	0.15	0.11	-0.89	0.01	0.02	0.01	0.02	0.01		0.31	0.67
2-4_b	0.14	0.17	0.13	-0.09	-0.87	-0.10	0.01	-0.03	0.02	-0.03		0.50
2-5_b	0.16	0.18	0.15	-0.02	-0.09	-0.88	0.02	-0.03	0.01	-0.04	0.04	

* _e, _b – postfixes of PDD and burnup, respectively.

– weak positive correlation, $r \in [0.15;0.30)$
– moderate positive correlation, $r \in [0.30;0.70]$
– moderate negative correlation, $r \in [-0.30;-0.70]$
– strong negative correlation, $r \in [-0.70;-1.00]$

Fig. 5. Kendall rank correlation coefficients and p-values.

3. MACHINE LEARNING PREDICTIVE MODEL

Based on identified relationships of data distributions, the most suitable machine learning paradigm for this study is supervised learning, that uses already tagged with the correct answer labeled datasets to train algorithms to predict outcomes and recognize patterns. The target feature to predict is PDD values in each cell ($N = 20$).

There are several algorithms used in supervised learning tasks, each with its own strengths and weaknesses. Therefore, in most studies, the choice of a training algorithm is entirely empirical [18–20]. To make initial assessment of the applicability of the training algorithms to predict PDD from burnup, the following were selected:

- ridge regression—linear regression with L2 regularization (penalty based on the absolute value of coefficients);
- LASSO regression—linear regression with L1 regularization (penalty based on the square of coefficients);
- Support vector machine (SVM);
- k-nearest neighbors (KNN);
- Gaussian process regression (GPR);
- gradient boosting regression (GBR).

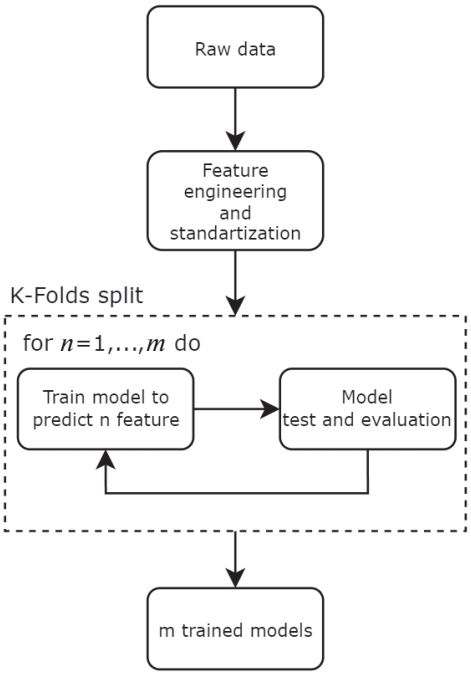

Fig. 6. General pipeline of models preparation.

Figure 6 presents the training pipeline, which includes data preprocessing, training, testing, and model evaluation.

On preprocessing stage, additional input features are generated to clarify difference between types of FAs (6-tube and 8-tube) in the reactor core. Then all features standardized relative to the mean and standard deviation to enhance the interpretability of the values. On training stage K-folds cross-validation technique is used to ensure that all observations from the original dataset have the chance to appear in both the training and test sets (Table 1). The output of pipeline is m-size array of trained models (model per cell approach). The performance of the training algorithms was assessed based on the coefficient of determination R^2 and mean absolute error (MAE).

It can be seen that L1 regularization is not applicable to the problem taks. In contrast, L2 regularization resulted in $R^2 = 0.95$, indicating the influence of the correlation relationship on the formation of the output feature. The SVM and KNN algorithms showed relatively low coefficients of determination, which can be attributed to the models sensitivity to data with a noise.

Table 1. Performance of machine learning algorithms

Model	R^2	MAE, %
Ridge	0.91	2.3
Lasso	0.01	97.1
SVM	0.71	5.5
KNN	0.55	7.0
GPR	0.95	1.9
GBR	0.88	2.8

The GBR model resulted relatively high accuracy, that can be improved by increasing model complexity (number of adjustable parameters). However, the generalization of such models may significantly deteriorate due to the risk of overfitting.

For further optimization task, the GPR model (Eq. (3)), which predicts a posterior Gaussian distribution determined by the covariance function k (Eq. (4)) was selected. The initial evaluation of GPR model (Table 1) was performed using the universal Radial Basis Function (RBF):

$$\begin{bmatrix} \mathbf{y^{tr}} \\ \mathbf{y^{te}} \end{bmatrix} \sim N\left(0, \begin{bmatrix} k(\mathbf{X^{tr}}, \mathbf{X^{tr}}) k(\mathbf{X^{tr}}, \mathbf{X^{te}}) \\ k(\mathbf{X^{te}}, \mathbf{X^{tr}}) k(\mathbf{X^{te}}, \mathbf{X^{te}}) \end{bmatrix}\right), \quad (3)$$

where $\mathbf{X^{tr}}$, $\mathbf{X^{te}}$—training and testing dataset of features, respectively; $\mathbf{y^{tr}}$, $\mathbf{y^{te}}$—training and testing dataset of labels, respectively:

$$Cov(\tilde{\mathbf{y}}^{\mathbf{te}}) = k(\mathbf{X^{te}}, \mathbf{X^{te}}) - \frac{k(\mathbf{X^{te}}, \mathbf{X^{tr}}) k(\mathbf{X^{tr}}, \mathbf{X^{te}})}{k(\mathbf{X^{tr}}, \mathbf{X^{tr}})}, \quad (4)$$

where $\tilde{\mathbf{y}}^{\mathbf{te}}$ is the prediction made on unseen data.

The kernel have a huge impact on the model's generalization that so for a comprehensive evaluation of the GPR properties, the main stationary covariance functions were considered: exponential, matern (3/2), and rational quadratic kernel, but all of them showed lower R^2 and MAE compared to the RBF (Eq. (5)):

$$k_{\text{RBF}} = \sigma^2_{\text{RBF}} \exp\left(-\frac{(\mathbf{X} - \mathbf{X}')^T (\mathbf{X} - \mathbf{X}')}{2\mathbf{I}}\right), \quad (5)$$

where $\mathbf{X}, \mathbf{X}'$ are the pairs of data; σ^2_{RBF} is the scale factor that determines the average distance from mean; $\mathbf{I}$ is the lengthscale.

Kernels can be combined by adding or multiplying them together to fully leverage their strengths and weaknesses for each data type. Multiplying kernels is an elementwise multiplication of their corresponding covariance matrices. This means that the covariances of the two multiplied kernels will only have a high value if both covariances have a high value (AND operator). On the other hand, two added kernels will only have a low value if both of the covariances have a low value (OR operation).

In present research we propose to combine RBF and white noise (WN) kernels by addition (Eq. (6))

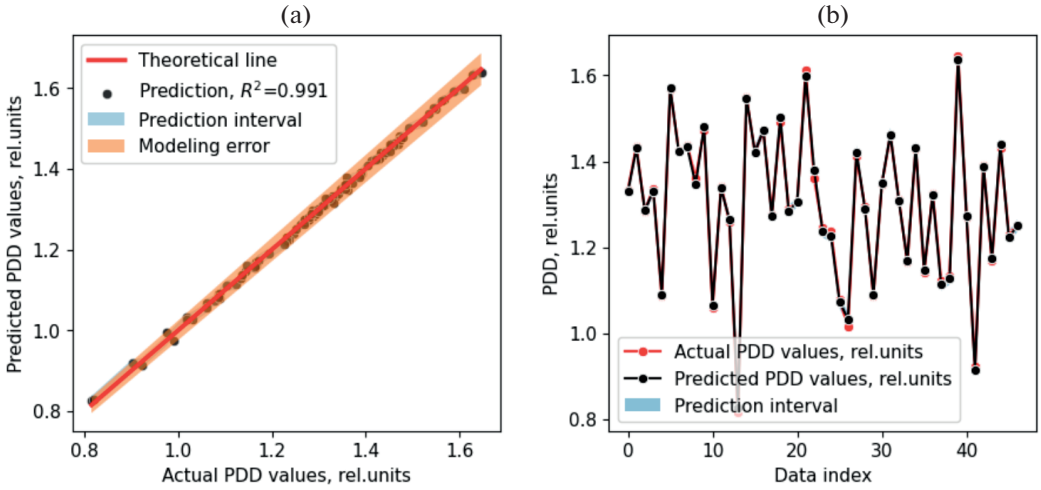

Fig. 7. Predictive ability of GPR model with combined kernel k_{add}: (a) actual and predictive values comparison; (b) predictions on test set.

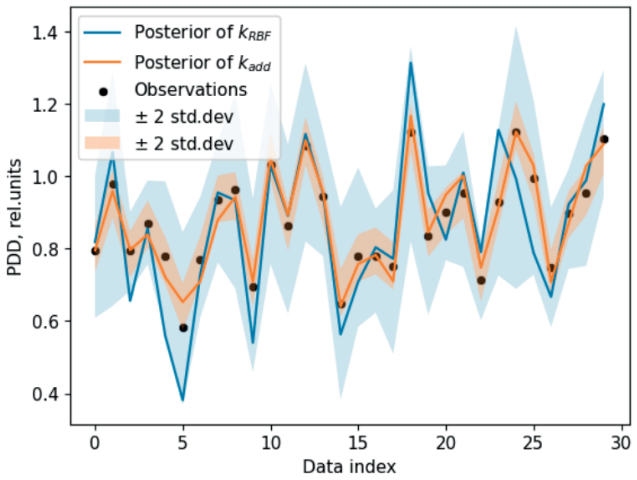

Fig. 8. Posterior Gaussian process for k_{RBF} and k_{add} kernels.

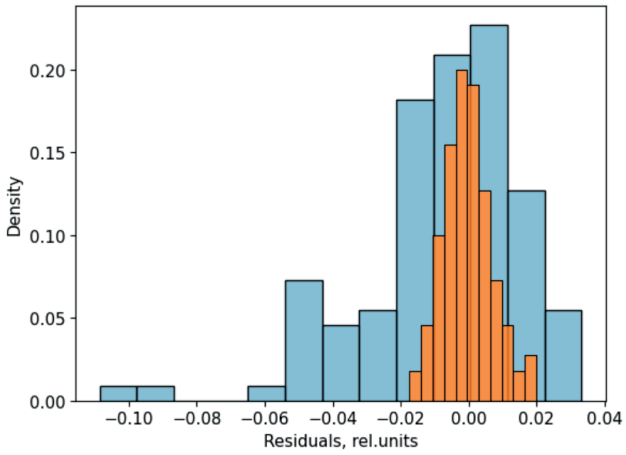

Fig. 9. Residuals comparison.

to improve GPR model performance and to reduce errors caused by multiple correlations between FAs.

$$k_{\text{add}} = k_{\text{RBF}} + \sigma_n^2 I_n, \tag{6}$$

where σ_n^2 is the variance of white noise; I_n is the identity matrix.

The white noise part of combined kernel results in a covariance matrix with zeros everywhere except on the diagonal of the covariance matrix. The independent and identically distributed variance σ_n^2 is added to the diagonal of the k_{RBF} kernel. Figure 7 presents the prediction results of the GPR model with the k_{add} kernel function.

It can be observed that the variance of the predicted values is small and does not exceed the range of modeling error. The coefficient of determination R^2 is 0.99 and MAE is 0.5%, which is more than three times lower than that of the initial model. The average processing time for a query and generation of a single pattern is no more than 50 ms.

Illustration of posterior Gaussian process with k_{RBF} and k_{add} kernels on samples drawn from distribution is presented in Fig. 8.

Standard deviation of Gaussian process with k_{add} kernel decreased by a factor of 3.3 compared to Gaussian process with k_{RBF} kernel. We also compared distributions of residuals of both GPR models Fig. 9 to show differences between the observed and estimated values.

To indicate the stability of model and quantify uncertainty of predictions the prediction intervals (PI) was estimated using Eq. (7). PIs can determine where the next data point sampled may appear and account for both the uncertainty of estimating

Monte Carlo tool MCU-PTR

Cell	6	5	4	3
7	0.72	1.00	1.20	1.01
6	0.81	1.29	1.02	0.95
5	1.17	Be	Be	0.96
4	1.16	Be	Be	0.94
3	0.83	0.98	1.26	0.89
2	0.71	1.14	0.97	0.97
	PDD by sides, rel.units			
	0.98		1.02	

GPR model with k_{add} kernel

Cell	6	5	4	3
7	0.74	1.01	1.17	1.02
6	0.84	1.31	1.03	0.95
5	1.17	Be	Be	0.96
4	1.18	Be	Be	0.94
3	0.83	0.97	1.27	0.89
2	0.72	1.11	0.94	0.95
	PDD by sides, rel.units			
	0.99		1.01	

Fig. 10. Comparison of PDDs obtained by use of MCU-PTR code and GPR model.

a value and the random variation of individual values sampled [16]:

$$\tilde{y} \pm z\sqrt{\frac{1}{n-2}\sum_{i}^{n}(\tilde{y}_i - y_i)^2}, \qquad (7)$$

where $\tilde{y}$ is the predicted value; z is the critical value from Gaussin distribution.

PI of GPR model with k_{add} kernel function at 95% significance level ($z = 1.96$) was determined to be 0.040 rel.units, indicating the stability of the model.

The series of real-life tests of GPR model with k_{add} kernel was applied in conjunction with the MCU-PTR code in the tasks of core refueling and nonuniformity power density profiling for the IRT-T reactor during the 2023–2024 fuel cycles. Figure 10 presents the PDD values obtained from calculations made in MCU-PTR code and the predictions of the GPR model for one of the IRT-T reactor fuel pattern.

The MAE of predicted values across the fuel cells in the core was 1.1%. No outliers in the predicted values were observed for any of the cells, confirming the stability of the algorithm's performance under real conditions.

Thus, the developed model is capable to predict PDD for the reactor core in a heterogeneous structure. The use of the combined covariance function allowed for the elimination of multiple correlations between the input and output features, that so overall accuracy of GPR model is increased up to 99%.

CONCLUSIONS

The partial refueling mode and the asymmetrical neutron reflector are the causes of a high degree of heterogeneity of neutronic parameters in the IRT-T reactor core.

An analysis of the IRT-T reactor's operational experience has shown that the PDD pattern for each fuel cell depends on the cell's location, fuel burnup depth, and neighboring FAs. In certain cases, the maximum difference in PDD between central and peripheral cells can reach 50–55%. Correlation analysis revealed that the PDD values in one cell are influenced by the most distant cells (PDD in cell 7-6 is determined by the burnup values in cells 2-3, 2-4, and 2-5).

To predict PDD values in each fuel cell, a system consisting of 20 machine learning models was used, with each model predicting values for only one cell. Based on the empirical evaluation of existing machine learning algorithms, the GPR model, based on Gaussian processes, demonstrated the highest accuracy (over 95%).

The GPR model was optimized by developing combined covariance function of RBF and WN. The optimized GPR model is capable of predicting PDD values in the heterogeneous structure of the reactor core with an overall accuracy of $R^2 = 0.99$. The MAE of model on test set across the core cells is 0.5%. Additionally, testing the model on series of real-life tasks showed that the MAE of the predictions does not exceed 1.1%.

The developed model predicts PDD values based on the fuel burnup data, allowing for the assessment of PDD changes in case of refueling and the evaluation of the effectiveness of FA permutation in the core without the need for resource-intensive calculations. The model has a high query processing speed, generating a single pattern in no more than 50 ms.

FUNDING

This work was supported by ongoing institutional funding. No additional grants to carry out or direct this particular research were obtained.

CONFLICT OF INTEREST

The authors declare that they have no conflicts of interest.

REFERENCES

1. V. A. Tsykanov, *The Effect of Fuel Partial Overloading on the Fuel Consumption and Cost in the Research Reactors* (SKIAR, Dimitrovgrad, Moscow oblast, 1973).
2. V. A. Starkov and Yu. B. Chertkov, *Calculated Model of SM Reactor and Results of Its Testing for Determination of Fuel Burnup and Fission Product Distribution* (IATE, Obninks, Kaluga oblast, 2011).
3. S. Suman, J. Cleaner Prod. **278**, 124022 (2021). https://doi.org/10.1016/j.jclepro.2020.124022
4. G. G. Glukhov and A. N. Didenko, Sov. At. Energy **64**, 423 (1998). https://doi.org/10.1007/bf01123281
5. N. I. Alekseev, E. A. Gomin, S. V. Marin, V. A. Nasonov, D. A. Shkarovskii, and M. S. Yudkevich, At. Energy **109**, 149 (2011). https://doi.org/10.1007/s10512-011-9337-0
6. Yu. B. Chertkov, M. N. Anikin, I. I. Lebedev, A. G. Naimushin, and N. V. Smol'nikov, At. Energy **131**, 42 (2021). https://doi.org/10.1007/s10512-022-00834-y
7. M. V. Shchurovskaya, V. P. Alferov, N. I. Geraskin, A. I. Radaev, A. G. Naymushin, Yu. B. Chertkov, M. N. Anikin, and I. I. Lebedev, Ann. Nucl. Energy **96**, 332 (2016). https://doi.org/10.1016/j.anucene.2016.06.015
8. M. V. Shchurovskaya, V. P. Alferov, N. I. Geraskin, A. I. Radaev, A. G. Naymushin, Yu. B. Chertkov, M. N. Anikin, and I. I. Lebedev, Ann. Nucl. Energy **113**, 436 (2018). https://doi.org/10.1016/j.anucene.2017.11.046
9. J. J. Ortiz-Servin, J. M. Cadenas, D. A. Pelta, A. Castillo, and J.-L. Montes-Tadeo, Ann. Nucl. Energy **80**, 236 (2015). https://doi.org/10.1016/j.anucene.2015.02.017
10. A. Thakur, D. Sarkar, V. Bharti, and U. Kannan, Ann. Nucl. Energy **150**, 107869 (2021). https://doi.org/10.1016/j.anucene.2020.107869
11. A. Pazirandeh and Sh. Tayefi, Ann. Nucl. Energy **42**, 112 (2012). https://doi.org/10.1016/j.anucene.2011.12.010
12. M. Yescas, B. Le Gloannec, and F. Roch, J. Nucl. Mater. **558**, 153360 (2022). https://doi.org/10.1016/j.jnucmat.2021.153360
13. L. P. Filho, K. C. Souto, and M. D. Machado, in *International Nuclear Atlantic Conference (INAC 2013)*, p. 12.
14. J. M. C. Contardo, X. A. Lopez-Cortes, and I. Merino, in *2021 40th International Conference of the Chilean Computer Science Society (SCCC), La Serena, Chile, 2021* (IEEE, 2021), p. 1. https://doi.org/10.1109/sccc54552.2021.9650410
15. A. L. Brophy, Behav. Res. Methods, Instrum., Comput., **18**, 45 (1986). https://doi.org/10.3758/bf03200993
16. S. Gupta, K. Saluja, A. Goyal, A. Vajpayee, and V. Tiwari, Measurement: Sensors **24**, 100432 (2022). https://doi.org/10.1016/j.measen.2022.100432
17. P. Giudici, A. Gramegna, and E. Raffinetti, Soc.-Econ. Plann. Sci. **87**, 101560 (2023). https://doi.org/10.1016/j.seps.2023.101560
18. N. K. Ahmed, A. F. Atiya, N. E. Gayar, and H. El-Shishiny, Econometric Rev. **29**, 594 (2010). https://doi.org/10.1080/07474938.2010.481556
19. C. E. Rasmussen and C. K. I. Williams, *Gaussian Processes for Machine Learning* (MIT Press, 2008).
20. D. L. Shrestha and D. P. Solomatine, Neural Networks **19**, 225 (2006). https://doi.org/10.1016/j.neunet.2006.01.012

AI tools may have been used in the translation or editing of this article.